RSC Advances

PAPER

View Article Online
View Journal | View Issue

Cite this: *RSC Adv.*, 2026, **16**, 28619

Supramolecular complexation of nanoclusters with a non-fluorinated polymer for proton exchange membranes at intermediate temperatures

Junjie Zhou,[ab] Shanshan Guo,[ab] Zihao Zhang,[ab] Chuanjin Zhao[ab] and Xinpei Li *[ab]

Intermediate-temperature proton exchange membranes (PEMs) offer various benefits in fuel cells, including simplified water and thermal management, enhanced fuel tolerance, and improved electrochemical kinetics. In this study, a Keggin-type nanocluster is complexed with polyvinyl alcohol *via* a simple solution-casting method, and glycerol is used as a plasticizer to enhance the mobility of polymer molecular segments. Owing to the oxygen-rich surface configuration and anionic surface charge, the well-defined nanoclusters engage in diverse intermolecular interactions with polymers. Furthermore, glycerol establishes hydrogen bonds with the polymer, reducing the crystallinity of the polymeric matrix. The proposed proton conductor exhibits a robust intermediate-temperature proton conductivity of 2.03 $\times$ 10^{-3} S cm^{-1} at 110 °C under anhydrous conditions. This work addresses the critical challenge of maintaining high proton conductivity under low-humidity conditions while ensuring thermal stability and mechanical integrity for PEMs at intermediate temperatures. Nevertheless, this simple solution-casting approach, based on the blending of Keggin-type nanoclusters and polymer *via* supramolecular interactions, is suitable for large-scale production.

Received 25th March 2026
Accepted 16th May 2026

DOI: 10.1039/d6ra02438f

rsc.li/rsc-advances

1. Introduction

Proton exchange membrane fuel cells (PEMFCs) represent a pivotal clean energy technology, characterized by high efficiency and environmental benefits, aligning with global goals for hydrogen economies and carbon neutrality. The PEM as the core component, critically determines the overall cell performance. Currently, perfluorosulfonic acid membranes (*e.g.*, Nafion) dominate the commercial landscape. However, their proton conduction relies heavily on water molecules, necessitating operation below 80 °C to prevent membrane dehydration, which leads to the collapse of hydrophilic ion channels and a severe decline in conductivity.[1–4] Operating PEMFCs at intermediate temperatures (100–120 °C) offers significant advantages, including simplified water/thermal management, enhanced tolerance to fuel impurities (*e.g.*, CO), and improved electrode kinetics. This underscores the urgent need to develop alternative PEM materials capable of maintaining high performance under such conditions.

Conventional strategies for intermediate-temperature PEMs, such as sulfonated aromatic polymers (*e.g.*, SPEEK, SPI) or phosphoric acid-doped polybenzimidazoles (PA–PBI), often face inherent trade-offs.[5–7] Sulfonated polymers typically suffer from drastic conductivity loss at low humidity,[8,9] while PA–PBI systems are prone to acid leaching during operation.[10,11] These limitations highlight the challenge of achieving a stable balance between proton conductivity, mechanical integrity, and durability under anhydrous or low-humidity intermediate-temperature conditions.

A class of well-defined, nanoscale metal–oxygen cluster anions polyoxometalates (POMs) have emerged as promising inorganic fillers.[12,13] Their unique properties, including strong Brønsted acidity, high proton mobility, exceptional thermal stability (>300 °C), and intrinsic hygroscopicity,[14,15] make them ideal candidates for facilitating proton transport, particularly in low-humidity environments.[16] However, their high water solubility and poor intrinsic film-forming ability present critical obstacles for their direct application as stand-alone membranes. To harness POMs in PEMs, a common strategy is to incorporate them into a polymer matrix. The significance of employing PVA with Keggin-type POMs becomes evident when compared to the prevalent strategies in POM/polymer hybrid PEMs. Many existing systems rely on fluorinated polymers (*e.g.*, Nafion) or expensive sulfonated engineering thermoplastics to ensure mechanical strength and processability,[17] which inevitably increases cost and environmental footprint. Other approaches involve complex covalent modification of POMs with perfluorinated polymers to enhance compatibility,[15] adding synthetic steps and complexity. These factors collectively underscore the need for a design that is simultaneously effective, simple, sustainable, and cost-efficient.

[a]*School of Machinery and Automation, Weifang University, Weifang 261000, China. E-mail: lixp@wfu.edu.cn*

[b]*Shandong Key Laboratory of Intelligent Manufacturing Technology for Advanced Power Equipment, Weifang University, Weifang 261000, China*

This work demonstrates a distinct strategy by employing foundational, low-cost polyvinyl alcohol[18,19] and introducing glycerol as a critical third component. While glycerol is valued for its humectant properties,[19–21] its novel role here is as a multifunctional supramolecular mediator designed specifically to prevent POM aggregation. This mediator functions by plasticizing the PVA matrix and, more importantly, by acting as a molecular bridge that co-constructs an extensive hydrogen-bonding network with both PVA's hydroxyl groups and the POM's surface oxygens. This synergistic design successfully achieves molecular-level dispersion of POMs, as confirmed by homogeneous morphology in SEM and SAXS/WAXS analyses. Therefore, the novelty of this work lies not merely in the ternary composition, but in the proposed and validated design principle centered on supramolecular homogenization. This principle, realized through glycerol-mediated hydrogen-bonding networks, provides a practical and sustainable pathway for developing durable, high-performance proton-exchange membranes.

2. Experimental

2.1 Materials and agents

Glycerol (industrial grade, ≥99.0%), polyvinyl alcohol (industrial grade, alcoholysis degree ≥ 98.5%), and Keggin-type phosphotungstic acid (industrial grade, ≥99.0%), all sourced from Aladdin Biochemical Technology Co., Ltd (Shanghai, China). The ultrapure water (resistivity 18.2 MΩ cm) was produced by a WaterPro system (Sichuan, China).

2.2 Characterization methods

Performance tests were conducted on the inorganic–organic hybrid PEMs.

The prepared materials were subjected to TGA tests in accordance with ISO 11358. Thermogravimetric analysis was performed using a TA Instruments 5500 thermogravimetric analyzer (USA). The test temperature ranged from 25 °C to 800 °C with a linear heating rate of 10 °C min^{-1} under a nitrogen atmosphere.

Broadband dielectric spectroscopy was carried out using an Alpha-A spectrometer from Novocontrol Technologies GmbH & Co. KG (Germany). The test temperature ranged from −80 °C to 120 °C with a heating rate of 5 °C min^{-1} under a nitrogen atmosphere.

Electrochemical workstation tests were performed using a CHI660E from CH Instruments (Chenhua). The initial voltage was set at 0 V with an amplitude of 0.005 V, and the frequency was swept from 106 Hz to 0.1 Hz.

Scanning electron microscopy (SEM) observations were conducted using an EM8000 microscope purchased from KYKY Technology Co., Ltd (Beijing Zhongke Keyi).

The film thickness was measured according to the ISO 4593:1993 standard using a Mitutoyo 547-400 digital thickness gauge.

2.3 Sample preparation process

The intermediate-temperature PEMs is prepared by a solution-casting method that is operationally simple and cost-effective. It is reported that PVA combined with Keggin-type POMs show high proton conductivity in high-humidity conditions. However, under dry gas conditions, the membrane's proton conductivity decreases sharply, and interfacial resistance increases dramatically, hindering the fuel cell's power output significantly. Glycerol can form hydrogen bonds with PVA, reducing its crystallinity. Additionally, glycerol is chemically compatible with PVA and POMs, which helps enhance the thermal stability of the membrane. In this work, glycerol, acting as a plasticizer and humectant, is incorporated to modulate the membrane's properties.

The synthesis procedure is shown in Scheme 1. Glycerol, PVA, and H_3PW_{12} are added in sequence with different proportions into a 20 mL glass tube containing of a magnetic stirrer. To comprehensively investigate the impact of different components on the performance of the prepared electrolyte, the following systematic optimization procedure will be implemented (Table 1), with each sample group requiring three separate batches of preparation to ensure the reproducibility and reliability of the experimental results. The mixture is stirred evenly at 60 °C. Then, the solution is cast onto a glassware until the water molecules evaporate. Finally, the film is peeled.

3. Results and discussion

3.1 Microstructure characterization

Fig. 1a shows an optical photograph of the optimal composite membrane (denoted as Example 3), demonstrating excellent transparency and bendable/flexible characteristics. This macroscopic homogeneity and mechanical flexibility directly result from the molecular-level integration of components and

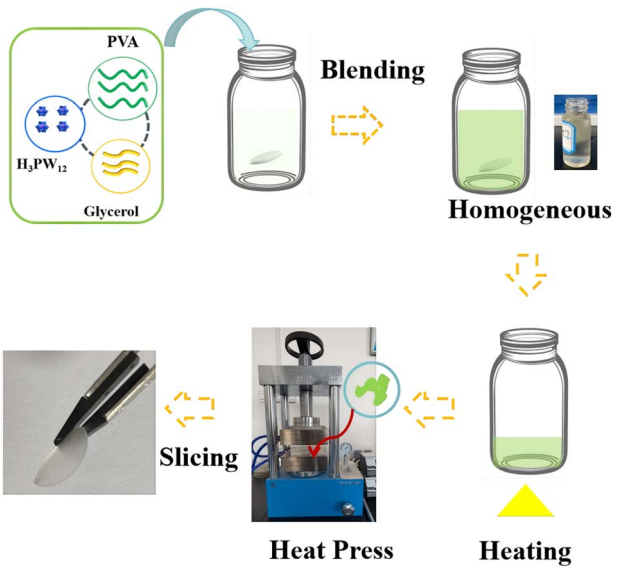

Scheme 1 The schematic diagram of the proposed electrolyte synthesis process.

Table 1 Different ratios of the three components

Example	Glycerol	PVA	PW
Example 1	1.5	2	0.5
Example 2	1.5	2	0.8
Example 3	1.5	2	1
Example 4	1.5	2	1.3
Example 5	1.5	2	1.5
Example 6	1.5	2	1.8
Example 7	2	3	1
Example 8	1	1	1
Control Example 1	1.5	2	0.3
Control Example 2	0.5	3	1
Control Example 3	3.4	0.1	1
Control Example 4	0.5	2	1
Control Example 5	1	2	1
Control Example 6	2	2	1

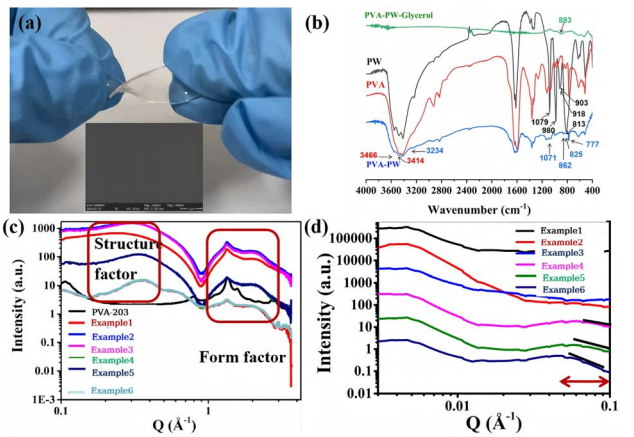

Fig. 1 (a) Optical image of the Example 3 sample; (b) SEM micrograph of Example 3; (c) WAXS patterns of samples with different POM contents; (d) SAXS profiles of samples with different POM contents.

the dynamic, reversible supramolecular interactions (*e.g.*, hydrogen bonding) within the composite network. To verify the intermolecular interactions among the components, comparative FTIR spectra of PW, PVA-203, PVA–PW composite, and Example 3 electrolyte were recorded (Fig. 1b). In the O–H stretching region (3700–3000 cm^{-1}), pristine PVA-203 exhibits bands at ~3466 and 3414 cm^{-1}, attributed to free and weakly hydrogen-bonded OH groups. Upon incorporation of PW, a new broad band centered at 3234 cm^{-1} appears, which is indicative of strongly hydrogen-bonded hydroxyls. This suggests the formation of robust H-bonds between the OH groups of PVA and the oxygen atoms of the Keggin anion. After further addition of glycerol, the O–H envelope becomes broader and more structured, indicating that glycerol hydroxyls also enter the hydrogen-bonding network. In the fingerprint region of the Keggin unit, pure PW shows characteristic bands at 1079 cm^{-1} (ν(P–O_a)), 980 cm^{-1} (ν(W=O_t)), 918/903 cm^{-1} (ν(W–O_β–W)), and 813 cm^{-1} (ν(W–O_c–W)). In the PVA–PW composite, the ν(W=O_t) disappears, while the ν(W–O_β–W) and ν(W–O_c–W) bands shift to 862, 825, and 777 cm^{-1}, respectively, and ν(P–O_a) moves to 1071 cm^{-1}. These red shifts indicate that the terminal and bridging W–O bonds are weakened due to hydrogen-bonding interactions between PVA hydroxyls and the external oxygen sites of the polyanion. In the ternary Example 3 electrolyte, the W–O–W absorption appears at 893 cm^{-1}, reflecting a reorganized H-bonding environment involving glycerol. Collectively, the FTIR results provide direct evidence for the hydrogen-bonding and other functional interactions that stabilize the composite electrolyte system.

As shown in the SEM image taken at a magnification of 10000× (Fig. 1a, inset), the designed polymer electrolyte exhibits a continuous and remarkably homogeneous morphology. It should be noted that no obvious phase separation was observed at this resolution. This observed structural integrity is crucial as it minimizes interfacial defects and percolation barriers which is beneficial for proton transport. Indeed, a high proton conductivity of 0.007 S cm^{-1} measured at 25 °C and 100% RH, as discussed in the sections "ionic transport properties". To gain deeper insights into the dispersion state of POM nanoclusters, their aggregation behavior, and their impact on polymer crystallinity,[22–24] we employed wide-angle X-ray scattering (WAXS) and small-angle X-ray scattering (SAXS). The WAXS profiles in Fig. 1c compare pristine PVA with composite membranes of varying POM content. The pristine PVA-203 exhibits sharp Bragg crystalline peaks at $Q \approx 1.5$ $Å^{-1}$, while in the spectra of examples, the peak intensity at Q near 1.5 $Å^{-1}$ is significantly reduced and other crystalline peaks associated with PVA disappear. This confirms that the strong intermolecular interactions (*e.g.*, hydrogen bonding and electrostatic forces) between the POM nanoclusters and the PVA chains effectively disrupt polymer chain ordering, thereby reducing crystallinity. This decrystallization enhances polymer segmental mobility, which is vital for facilitating proton conduction.

In the WAXS profiles of Examples 1–5, the scattering signal arises from two distinct contributions. The form factor of individual Keggin-type POM clusters governs the overall shape of the scattering curve at intermediate Q, and the structure factor reflects the inter-cluster spatial correlation and produces a low-Q shoulder/peak. The clear presence of both features allows us to distinguish the intra-cluster structure from the inter-cluster ordering. The WAXS profile of Example 1 reveals an intact form factor of Keggin-type POM, with no prominent Bragg peaks in the structure factor, indicating a homogeneous, molecular-level dispersion of POM within the polymer matrix. As the POM content increases, the structure factor exhibits a broadened peak whose position shifts toward higher Q values, indicating the formation of POM-enriched domains within the polymer matrix and a gradual reduction in inter-POM distances.

The SAXS profiles of Examples 1–3 exhibit no distinct peaks near $Q \approx 0.1$ $Å^{-1}$ (Fig. 1d), indicating the presence of amorphous aggregation of POM clusters. While the SAXS curves of Examples 4 and 5 display a consistent slope of approximately −2 in that Q-region. This behavior suggests that the POM units undergo dynamic cross-linking to form a percolated network.[25] While such a network may increase the tortuosity of proton transport pathways, it also establishes a contiguous matrix of

hopping sites for protons. A further increase in POM loading (Example 6) changes the slope of the SAXS curve near $Q \approx 0.1$ Å^{-1} to approximately −3, implying that partial POM aggregation occurs to generate dense cores with rough interfaces likely due to reduced miscibility between POM and the polymer matrix at high POM concentrations. In summary, this hierarchical structural evolution from molecular dispersion to a percolated network and finally to dense aggregates is precisely modulated by the POM content. It highlights the critical role of supramolecular complexation in governing the nano- and microstructure of the nanocluster/polymer composite, which in turn dictates the proton conduction mechanisms and overall performance of the membrane.

3.2 Thermal stability

The thermal stability of PEMs is paramount for their practical application at intermediate temperatures. Fig. 2 presents the thermogravimetric analysis (TGA) and differential scanning calorimetry (DSC) results, systematically evaluating the influence of POM content on the thermal properties of the supramolecular composites. As shown in the TGA curves (Fig. 2a), all composite electrolytes exhibit excellent thermal stability within the target operational range. All the composite electrolytes exhibited two-stage degradation process. The composite electrolytes exhibit negligible mass loss (<0.5%) across all tested samples from 25 °C to 110 °C, indicating excellent thermal stability for intermediate-temperature applications without significant decomposition or dehydration. The first degradation stage (temperature from 200 °C to 300 °C) corresponds to the decomposition of PVA backbone and glycerol (the cleavage of C–O bonds) and the evaporation of a small amount of bound water. The second stage (temperature from 350 °C to 450 °C) corresponds to the further degradation of the molecular chains of PVA and glycerol. A notable finding is the role of POM nanoclusters in enhancing the thermal robustness of the non-fluorinated polymer matrix. For instance, the thermal degradation process of the Example 1 with 18.6 wt% POM shows that the overall mass residue exceeds 30% at 800 °C, significantly higher than that expected from the inorganic content alone. This indicates that POM incorporation protects the PVA matrix. The residual mass initially increases with POM content, reaching a maximum, and then decreases at higher loadings. This reduction is attributed to POM agglomeration, which weakens the interfacial interaction between POM and PVA, leading to a decrease in mass residue. The influence of POM on polymer chain dynamics is further elucidated by DSC (Fig. 2b). The glass transition temperature (T_g) decreases slightly as the POM content increases from 12.5 wt% to 27.8 wt%. At low POM contents, POM acts as a plasticizer, increasing the flexibility and mobility of PVA chains, thereby reducing T_g. However, beyond a critical concentration, further POM addition leads to an increase in T_g. At high loadings, POM tends to agglomerate, forming high-concentration zones that trigger cross-linking reactions, restricting chain mobility and thus increasing T_g.

In summary, the thermal analysis reveals that the supramolecular complexation strategy yields composites with adequate stability for intermediate-temperature fuel cells. The POM nanoclusters play a dual role in enhancing thermal residual stability at optimal dispersions and critically modulating the viscoelastic properties of the polymer matrix, which is intrinsically linked to proton transport mechanism.

3.3 Ionic transport properties

To evaluate the bulk and interfacial ion-transport properties of the nanocomposites, electrochemical impedance spectroscopy (EIS) was employed. We employed a symmetric two-electrode configuration with identical silver foils to ensure a uniform current distribution. The membrane was firmly clamped between the electrodes, and the contact pressure was kept constant for all samples to ensure reproducibility. Membrane thickness was measured at multiple points using a digital micrometer. All measurements were conducted inside a temperature and humidity-controlled chamber. Before each measurement, the membrane was equilibrated under the target temperature and humidity for at least 2 hours. Nyquist plots for membranes with varying POM content are presented in Fig. 3a. The spectra were fitted using equivalent circuit fitting to determine the bulk ionic resistance (R_s) and the interfacial charge-transfer resistance (R_{ct}). As shown in Table 1, we compared Example 3 and control samples (Control 4–6), which have glycerol concentrations of 14.3%, 25%, 33.3%, and 40%, respectively. The corresponding R_s and R_{ct} values obtained from EIS analysis are summarized in Table 2 and Fig. S10. It is evident that the polymer electrolyte with a glycerol concentration of 33.3% (Example 3) exhibits the highest proton conductivity. Glycerol likely acts as a multifunctional component. Primarily, it serves as a plasticizer for the PVA matrix, increasing polymer chain flexibility and segmental mobility, which is crucial for facilitating proton transport. Furthermore, its

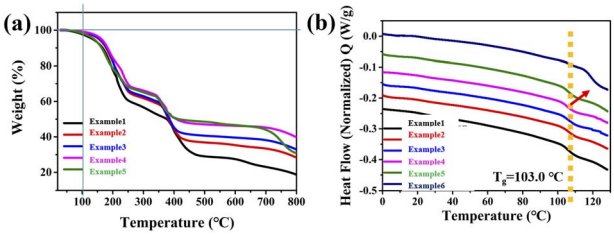

Fig. 2 (a) TGA curves of samples with different POM contents; (b) DSC curves of samples with different POM contents.

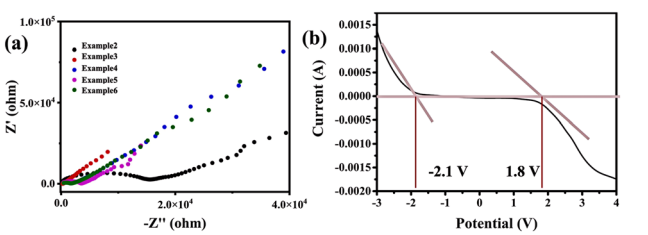

Fig. 3 (a) EIS spectra of samples with different POM contents; (b) LSV curves of the supercapacitor assembled with P(H)PG-3.

Table 2 Measured thickness, R_s, R_{ct}, and proton conductivity for each sample

Example	Membrane thickness (μm)	R_s (ohm)	R_{ct} (ohm)	σ (S cm^{-1}) (30 °C)
Example 1	2000	301.8	2650	8.44×10^{-4}
Example 2	2000	134.3	14 461	1.89×10^{-3}
Example 3	2000	133.3	144.7	1.91×10^{-3}
Example 4	2000	270.6	1383	9.41×10^{-4}
Example 5	2000	214.7	3149	1.18×10^{-3}
Example 6	2000	337.9	1310	7.54×10^{-4}
Example 7	200	388.1	98 063	6.56×10^{-5}
Example 8	200	198.7	5360	1.28×10^{-4}
Control Example 1	200	177.2	7512	1.43×10^{-4}
Control Example 2	200	122.6	23 798	2.07×10^{-4}
Control Example 3	—	—	—	—
Control Example 4	5000	600.3	2908	1.06×10^{-3}
Control Example 5	5000	471.8	404.8	1.35×10^{-3}
Control Example 6	5000	320.8	154.4	1.98×10^{-3}

hydroxyl groups function as proton-hopping sites and participate in constructing a continuous hydrogen-bonding network with both PVA and POMs. This network not only enables efficient proton conduction pathways but also helps to homogenize the dispersion of POM clusters, preventing their aggregation and thereby reducing ionic resistance. The existence of an optimal concentration (33.3%) indicates that a balance is achieved between sufficient proton-conducting pathways and maintained mechanical integrity of the membrane.

From Examples 1 to 6, he polymer electrolyte exhibits a large, depressed semicircular arc at the medium-to-low frequency region at low POMs content, suggesting a relatively high R_{ct} at the electrode/electrolyte interface. However, the intercept of the semicircle with the Z' axis at the high-frequency indicates a certain bulk resistance, implying that the POMs effectively disrupt the segmental ordering of PVA chains while leaving residual crystalline domains incompletely suppressed. As the POM content increase, the semicircle arc shifts toward the lower impedance region accompanied by a diminishing arc radius, signifying a simultaneous reduction in both R_{ct} and R_s. This enhancement is attributed to the progressive disruption of PVA chain ordering by the growing POM population. A higher population of POM facilitates the formation of percolated, three-dimensional networks that effectively lower the activation energy for proton conduction through optimized ionic hopping pathways. Based on the EIS spectra and equivalent circuit fitting (Fig. 3a, S3–S8 and Table 2), Example 3 was identified as the optimal composition, exhibiting the smallest semicircle arc and the lowest high-frequency intercept, which correspond to minimal R_{ct} and bulk ionic resistance R_s, respectively. The proton conductivity of Example 3 (with a thickness of 0.5 cm) was subsequently quantified under standard conditions of 25 °C and 100% relative humidity (RH). The corresponding Nyquist plot is provided in Fig. S9. The calculated proton conductivity reached 0.007 S cm^{-1}. Compared with other non-fluorinated polymer membranes in Table 3 under similar conditions (without fillers and near room temperature), our membrane shows comparable or even better proton conductivity. The only exception is the LDH/PES system, which was measured at 80 °C and with filler incorporation, and both factors are known to significantly enhance proton conductivity. Thus, the higher conductivity in that specific work does not diminish the merit of our filler-free, room-temperature membrane. To further evaluate the sample's potential for practical fuel cell applications, an alternating temperature and humidity test was conducted. Herein are provided the EIS of Example 3 (Fig. S11 and S12), obtained after ten alternating cycles under 35% relative humidity at 25 °C and 100% RH at 100 °C. After ten cycles, the R_s values of the sample at 100 °C and 100% RH were 0.69 Ω and 0.84 Ω for the first and tenth cycles, respectively. This minimal change in R_s under alternating humidity and temperature conditions indicates good stability, laying a foundation for its potential application in practical fuel cells.

The composite demonstrating optimal conductivity and minimal interfacial resistance (Example 3) was selected for further evaluation of its electrochemical stability. Linear sweep voltammetry (LSV) aimed to determine its electrochemical stability window (ESW), defined as the voltage range within which no significant oxidative/reductive decomposition of the electrolyte occurs. The conventional aqueous electrolytes typically exhibit electrochemical decomposition potentials around 1.23 V (limited by water splitting),[31,32] while the assembled symmetric supercapacitor demonstrates an extended ESW spanning from −2.1 V to +1.8 V. Furthermore, to assess the long-term stability within this window, we performed thousands of charge–discharge cycles (Fig. S13), which demonstrated excellent capacitance retention. This remarkable expansion is attributed to the synergistic effects of humectant glycerol, PVA, and redox-reversible POM, which collectively suppress hydrogen/oxygen evolution reactions through multiple mechanism.

In addition, we employed broadband dielectric spectroscopy (BDS) to investigate the relationship between ion conduction and the segmental dynamics of molecular chains in the Example 3 electrolyte. Fig. 4a displays the frequency dependence of the real part of conductivity $\sigma'(f)$ for the Example 3 across the temperature from −80 °C to 120 °C. A clear distinction can be drawn between the ion transport mechanisms of

Table 3 A comparison between different systems

Filler type	Polymer	Preparation method	Operating temperature (°C)	RH (%)	Proton conductivity (S cm^{-1})	Ref.
Montmorillonite	SPEEK	Casting-evaporation process	Room	100	0.000704	26
Montmorillonite	PVOH	Casting-evaporation process	Room	100	0.0060	27
LDH	PES	Casting-evaporation process	80	100	0.33	28
Montmorillonite	SPSU	Casting-evaporation process	25	—	0.000511	29
None	PEG	Hydrothermal method	100	—	0.000012	30
None	PVA	Casting-evaporation process	25	100	0.007	This work

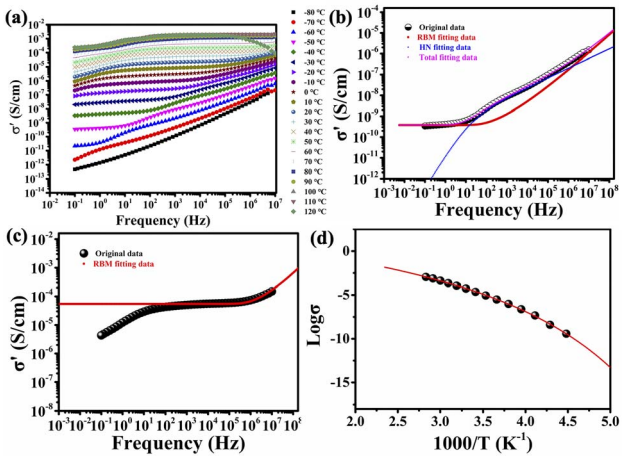

Fig. 4 (a) Conductivity-frequency spectra of the Example 3 sample at temperatures ranging from −80 °C to 120 °C; (b) conductivity-frequency spectrum of Example 3 at −60 °C with fitting curves based on the HN and RBM; (c) conductivity-frequency spectrum of Example 3 at −60 °C fitted with the RBM model; (d) temperature dependence of the conductivity of Example 3 and the corresponding VFT fitting curve.

Example 3 with temperature, directly linked to the mobility of the non-fluorinated polymer matrix.

At low temperatures (from −80 °C to −70 °C), where polymer segmental motion is highly restricted, proton conduction is governed by the localized segmental rearrangements. Proton migration occurs predominantly through hopping between confined sites, a process dependently on thermal activation to overcome inherent energy barriers. This frequency-dependent transport mechanism exhibits strong sensitivity to alternating electric field frequencies, as evidenced by the dispersion characteristics in conductivity spectra. At elevated temperatures (from −60 °C to 120 °C), intensified segmental mobility unlocks a different conduction mode. This dynamically disordered chain segments establish percolation pathways that enable long-range migration. This transition leads to the emergence of frequency-independent conductivity plateaus in the low-frequency regime. The onset and growth of this plateau signify a transition from localized hopping to a more fluid, long-range transport mechanism.

To quantitatively analyze this behavior, the spectra acquired within the temperature range of −60 °C to −40 °C were fitted using the Rouse–Bueche–Zimm (RBM) and Havrilliak–Negami (HN) models to determine the plateau conductivity (σ_0) and dielectric relaxation parameters (αH_3O^+). Fig. 4b displays the representative model fitting curves for the −60 °C spectrum, demonstrating the quantitative agreement between experimental data and theoretical formalism. The dielectric spectra spanning the temperature range from −30 °C to 120 °C were analyzed through comprehensive fitting with the RBM model to extract temperature evolution of σ_0 (Table S1 and Fig. 4c). Fig. 4d demonstrates the temperature-dependent evolution of proton conductivity, through the representation of $\log \sigma_0$ *versus* $1000/T$, following the Vogel–Fulcher–Tammann (VFT) equation $\sigma = \sigma_0 \exp\frac{-B}{T - T_0}$. According to the VFT equation fitting, we obtained $\log \sigma_0 = 1.45$, $B = 2212.29$ K, and $T_0 = 134.835$ K. Here, σ_0 is the pre-exponential factor representing the theoretical ionic conductivity at infinite temperature, B is the pseudo-activation energy parameter related to the energy barrier for ion migration, and T_0 is the Vogel temperature corresponding to the ideal glass transition temperature where configurational entropy becomes zero. The relatively large σ_0 indicates the presence of abundant mobile ions in this system, with a high-temperature limiting conductivity of 28.18 S cm^{-1}. The significant deviation between the Vogel temperature T_0 and the glass transition temperature ($T_g \approx 376.15$ K) measured by DSC for this polymer electrolyte is attributed to the addition of glycerol as a plasticizer. The glycerol creates a local "T_g" that is much lower than the T_g of the polymer matrix, indicating that the system is in a state of significant decoupling between ionic conduction and polymer segmental motion. Critically, Example 3 demonstrates a proton conductivity of 2.03×10^{-3} S cm^{-1} at 110 °C under anhydrous conditions. This performance underscores the effectiveness of the designed nanocluster-polymer composite as a promising PEM for fuel cells operating beyond the traditional temperature limits.

For proton-conducting polymer electrolyte systems, where proton conductivity or long-range proton migration dominates, the conventional dielectric loss spectra may be obscured by the overwhelming contribution of ionic polarization, thereby masking relaxation peaks associated with other molecular motions.[33,34] While the electric modulus ($M^* = 1/\varepsilon^*$) inherently suppresses the masking effect of long-range ionic conduction in the low-frequency regime, we employ the modulus loss formalism (*i.e.* the frequency-dependent plot of the imaginary part of the electric modulus $M''(f)$).[35,36] This allows for a clearer resolution of the intrinsic dipolar and localized charge relaxations within the supramolecular complex.

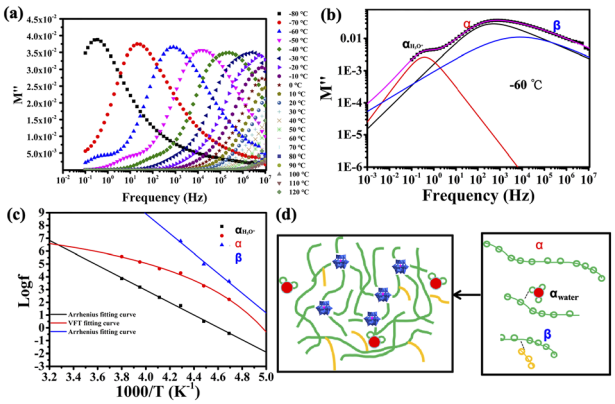

Fig. 5 (a) Electric modulus-frequency spectra of the Example 3 sample across temperatures ranging from −80 °C to 120 °C; (b) electric modulus-frequency spectrum of Example 3 at −60 °C fitted with three HN equations; (c) temperature dependence of distinct structural relaxation processes; (d) schematic illustration of the proposed microstructure of the sample and its relaxation behavior.

In the modulus loss *versus* frequency spectrum recorded at −60 °C (Fig. 5a), three distinct relaxation peaks are observed. These are attributed to the following dynamic processes within Example 3. The peak at highest frequency is assigned to the localized motion of polar side groups and glycerol chain segments (β-relaxation). The peak at intermediate-frequency reflects the cooperative segmental dynamics of the polymer backbone (α-relaxation). The peak at low frequency is associated with the short-range hopping of hydrated ions (αH_3O^+). To quantitatively deconvolute these overlapping relaxation processes, three Havriliak–Negami (HN) equations were employed to fit the experimental data (Fig. 5b). From the fitting, the characteristic frequency f_{max} of each relaxation peak was extracted across a wide temperatures range. The temperature dependence of these relaxation rates provides deep insight into their governing dynamics. Since the localized segmental motions (β-relaxation) and short-range hopping of hydrated ions (αH_3O^+) are thermally activated processes, their dynamic behaviors can be described by a single activation energy barrier. Consequently, these two processes obey the Arrhenius equation (Fig. 5c). As clearly demonstrated in the spectra, the segmental motion of the polymer backbone adheres to the VFT equation (Fig. 5c). This behavior is characteristic of the cooperative motions that require the simultaneous conformational rearrangements of multiple chain segments and are governed by the available free volume within the polymer matrix.

4. Conclusions

In conclusion, this study demonstrates a promising strategy for developing intermediate-temperature PEMs based on a sustainable, fully non-fluorinated hybrid system of PVA, POMs, and glycerol. The work provides significant mechanistic insight into how supramolecular complexation creates proton channels and couples polymer dynamics to transport. While the absolute proton conductivity is moderate, the composite achieves a balanced and relevant combination of properties; it exhibits mechanical flexibility, capability for low-humidity operation, and a wide electrochemical stability window, all of which are advantageous for intermediate-temperature applications. This fundamental understanding establishes a platform for future optimization. Further research is needed to explore alternative POM derivatives or novel polymer matrices to enhance proton conductivity while maintaining this favorable stability profile.

Author contributions

Junjie Zhou: investigation, data curation, visualization, writing-original draft. Shanshan Guo: writing original draft and methodology, funding acquisition. Zihao Zhang: data curation. Chuanjin Zhao: writing-review and editing. Xinpei Li: project administration, writing-review and editing, supervision, funding acquisition.

Conflicts of interest

There are no conflicts to declare.

Data availability

The data supporting this article have been included as part of the supplementary information (SI). Supplementary information additional TGA, EIS, CV data, and a conductivity table. See DOI: https://doi.org/10.1039/d6ra02438f.

Acknowledgements

The work is financially supported by Shandong Provincial Natural Science Foundation (Grant No. ZR2023QB149), Scientific Startup Foundation for Doctors of Weifang University (Grant No. 2023BS40), and National Natural Science Foundation of China (Grant No. 52107231).

References

1 K. Charradi, Z. Ahmed, R. E. Cid, P. Aranda, E. Ruiz-Hitzky, P. Ocon and R. Chtourou, *Int. J. Hydrogen Energy*, 2019, **44**, 10666–10676.
2 N. Brandau and J. Köhler, in *Springer Handbook of Electrochemical Energy*, ed. C. Breitkopf and K. Swider-Lyons, Springer Berlin Heidelberg, Berlin, Heidelberg, 2017, pp. 287–312, DOI: 10.1007/978-3-662-46657-5_10.
3 P. C. Okonkwo, I. Ben Belgacem, W. Emori and P. C. Uzoma, *Int. J. Hydrogen Energy*, 2021, **46**, 27956–27973.
4 R. Borup, J. Meyers, B. Pivovar, Y. S. Kim, R. Mukundan, N. Garland, D. Myers, M. Wilson, F. Garzon, D. Wood, P. Zelenay, K. More, K. Stroh, T. Zawodzinski, J. Boncella, J. E. McGrath, M. Inaba, K. Miyatake, M. Hori, K. Ota, Z. Ogumi, S. Miyata, A. Nishikata, Z. Siroma, Y. Uchimoto, K. Yasuda, K. Kimijima and N. Iwashita, *Chem. Rev.*, 2007, **107**, 3904–3951.

5 T. K. Maiti, J. Singh, J. Majhi, A. Ahuja, S. Maiti, P. Dixit, S. Bhushan, A. Bandyopadhyay and S. Chattopadhyay, *Polymer*, 2022, **255**, 125151.
6 M. Vinothkannan, E. K. Gikunoo and S. Shanmugam, *Ionics*, 2026, **32**, 57–68.
7 Y. Wang, Y. Luo, R. Chen, B. Sun, H. Liu, J. Wang, C. Gong and Q. Zhang, *Int. J. Hydrogen Energy*, 2024, **95**, 630–640.
8 J. Lou, Y. Lu, D. Yang, X. Pan, B. Li and P. Ming, *Int. J. Hydrogen Energy*, 2024, **94**, 756–764.
9 X. Xu, R. Li, C. Tang, H. Wang, X. Zhuang, Y. Liu, W. Kang and L. Shi, *Carbohydr. Polym.*, 2018, **184**, 299–306.
10 T. Chen, L. Chen, Y. Zhao, J. Hao and Z. Shao, *J. Membr. Sci.*, 2024, **707**, 122948.
11 M. Zhou, A. Ali, J. Zhu, S. S. Araya and V. Liso, *J. Power Sources*, 2024, **623**, 235411.
12 N. I. Gumerova and A. Rompel, *Nat. Rev. Chem.*, 2018, **2**, 0112.
13 X.-Q. Ma, H.-P. Xiao, Y. Chen, Q.-S. Lai, X.-X. Li and S.-T. Zheng, *Coord. Chem. Rev.*, 2024, **510**, 215818.
14 T. Iwano, S. Miyazawa, R. Osuga, J. N. Kondo, K. Honjo, T. Kitao, T. Uemura and S. Uchida, *Commun. Chem.*, 2019, **2**, 9.
15 F. Zhu, C. Wang, M. Tang, Z. Zheng, H. Yan and S. Chen, *Adv. Funct. Mater.*, 2024, **34**, 2408118.
16 R.-L. Liu, Y. Chen, X. Su, W. Zhu, Z. Liu, Y. Chen, D.-Y. Wang and G. Li, *Coord. Chem. Rev.*, 2025, **522**, 216224.
17 H. He, S. Song, L. Zhai, Z. Li, S. Wang, P. Zuo, Y. Zhu and H. Li, *Angew. Chem., Int. Ed.*, 2024, **63**, e202409006.
18 G. Arora, N. S. Sabran, C.-W. Liew, C. Y. Ng, F. W. Low and H. K. Jun, *Ionics*, 2024, **30**, 8073–8085.
19 C. Wong, W. Wong, K. Loh, W. Daud, K. Lim, M. Khalid and R. Walvekar, *Polym. Rev.*, 2020, **60**, 171–202.
20 Z. Gao, L. Han, J. Wan, G. Fu, X. Yang, Q. Guo, X. Ji, W. Chu, H. Tian and M. Lai, *Arab. J. Chem.*, 2024, **17**, 105789.
21 Y. Li, H. Chengxin, J. Lan, B. Yan, Y. Zhang, L. Shi and R. Ran, *Polymer*, 2020, **186**, 122027.
22 B. Jing, M. Ferreira, K. Lin, R. Li, B. M. Yavitt, J. Qiu, M. Fukuto and Y. Zhu, *Macromolecules*, 2020, **53**, 10972–10980.
23 X. Li, Z. Wang, C. Hong, F. Feng, K. Yu and H. Liu, *Macromolecules*, 2022, **55**, 9583–9593.
24 L. Hong-wei, C. Xiao-fang, Z. Jie, L. Xiang-dan and L. Li-Zhong, *Acta Polym. Sin.*, 2014, **014**, 115–121.
25 T. Li, A. J. Senesi and B. Lee, *Chem. Rev.*, 2016, **116**, 11128–11180.
26 J. Jaafar, A. F. Ismail, T. Matsuura and K. Nagai, *J. Membr. Sci.*, 2011, **382**, 202–211.
27 P. Bahavan Palani, R. Kannan, S. Rajashabala, S. Rajendran and G. Velraj, *Ionics*, 2015, **21**, 507–513.
28 N. H. Kim, A. K. Mishra, D.-Y. Kim and J. H. Lee, *Chem. Eng. J.*, 2015, **272**, 119–127.
29 M. G. Prasad, S. Mohanty and S. K. Nayak, *High Perform. Polym.*, 2014, **26**, 578–586.
30 M. Tsuboi, M. Hibino, N. Mizuno and S. Uchida, *J. Solid State Chem.*, 2016, **234**, 9–14.
31 Y. Qian, L. Su, H. Jing, C. Chai, F. Xie, X. Qiu and J. Hao, *Carbon Energy*, 2025, **7**, e697.
32 H. Qin, J. Zhang, H. Cheng, L. Hong, Z. Yang and X. Zhang, *Energy Fuels*, 2022, **36**, 9295–9302.
33 M. E. Córdova-Chávez, M. Hernández, S. J. Picken and E. M. Kelder, *ChemistrySelect*, 2018, **3**, 2931–2942.
34 J. You, B.-Y. Li, W. De Borggraeve and M. Wübbenhorst, *J. Chem. Phys.*, 2023, **159**, 164503.
35 P. B. Macedo, C. T. Moynihan and R. Bose, *Phys. Chem. Glasses*, 1972, **13**(6), 171–179.
36 C. T. Moynihan, R. D. Bressel and C. A. Angell, *J. Chem. Phys.*, 1971, **55**(9), 4414–4424.